**University of Bath**

**Alternative formats**

If you require this document in an alternative format, please contact:
openaccess@bath.ac.uk

# Regional admittivity reconstruction with multi-frequency complex admittance data using contactless capacitive electrical tomography

Gege Ma, and Manuchehr Soleimani

*Abstract*—Tomographic imaging of the electrical properties distribution within biological subjects such as the human body has been an active research goal in electrical tomography (ET). As the electrical properties of a living tissue vary with the excitation frequency, measuring the frequency-dependent behaviour of the effective dielectric can increase the possibilities for tissue characterisation, and thus enhance the potential for extended clinical applications. The ET system generally enables to capture the changes in effective dielectric properties at low spatial resolution, therefore, the complete complex admittance spectrum can be reconstructed by ET to enrich the information content and further provide better diagnostic. In this work, we demonstrate a novel contactless ET system which relies on the capacitive coupled principle, the capacitive coupled electrical tomography (CCET). Except the non-contact measuring characteristic, the capacitance-based imaging principle enables the system to obtain the measurements at higher excitation frequencies. These characteristics give CCET great potential in future medical application, as the high-frequency component of complex impedance plays a dominant role in establishing the link between the microscopic cell structures and the macroscopic admittivity images obtained from multi-frequency ET systems. In this paper, we used multi-frequency electrical signals from 320 kHz to 14 MHz to conduct the single and multiple inclusions test with different biological samples. Both the reconstructed tomographic images and the Cole-Cole plots confirm the ability of CCET in characterising different objects.

*Index Terms*—Cole-Cole Plots, Capacitive Coupled Electrical Tomography (CCET), Regional Admittivity imaging, Tissue Characterisation, Spectroscopy Tomography
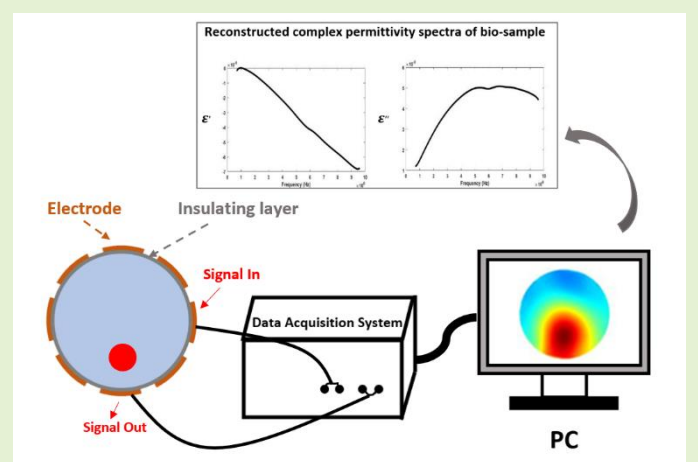
## I. Introduction

Bioelectrical properties are mainly determined by the cell's type, size, composition, viability, and metabolism. Therefore, bioelectrical impedance/admittance, which is able to reflect the physiological and pathological conditions of cells/tissues, has been widely used to characterize cells/tissues in a non-invasive way [1-4]. As the enclosed structure of the biological cell is made up by the multiple membranes controlling the movements of the ions inside and outside the cell, the membranes of cells can be electrically equivalent as the capacitor. On the two sides of the cell membrane, the intracellular fluid (ICF) and extracellular fluid (ECF) exists, which are equivalently regarded as the electrical resistance [5]. With the existence of cellular membrane, the electrical properties of bio-tissues at the excitation frequency ranging from a few Hz to several MHz show a variable and distinct response over the frequency. Consequently, the bio-impedance spectra analysis attracts growing interests in biological and medical applications as it enables to provide the complex impedance/admittance of the bio-tissues under the AC electrical signal [6-9].

There are many studies with biopsy data showing that the tumour tissues have a significantly different conductivity and permittivity from their surrounding normal tissues [10-11]. Delineation of the spectral characteristics of excised breast tissue has been provided by Jossinet and Schmitt [12] who measured complex admittivity in a range of frequencies. The samples of normal tissues (mammary glandular, connective, and adipose tissue), and three pathological groups (general mastopathy, fibroadenoma, and carcinoma) were excised during the test. Electrical information of these tissues was then

analysed by plotting the admittivity spectra and extracting specific parameters from these spectra. The combinations of the extracted parameters yield not only quantitative but also statistically discriminations among the different tissue samples, where the unique parameters of carcinoma tissues and normal tissues exist great difference. This high "contrast" in tissue electrical properties, occurring between a few kilohertz and several megahertz, can support the techniques relying on bioimpedance to differentiate malignant from benign tissues.

Previous study has shown the ability of electrical impedance spectroscopy (EIS) to roughly localize and clearly distinguish cancers from normal tissues and benign lesions [13-14]. EIS is an imaging technique for multi-frequency bio-impedance measurements, which enables to image the distributions of conductive and dielectric properties within the region of interest (ROI). After applying a multi-frequency time-varying current in the EIS system, the internal distribution of the bio-tissues can be reconstructed through the boundary electrical measurements from the electrode array-set [15]. EIS has the advantages of non-invasive, low-cost, and fast response, while one needs to note that the EIS requires a direct contact between the electrodes and the testing object. For medical application, the contact impedance can be a problematic as the electrode position and boundary movement may cause artefacts and bring errors.

In 2013, based on the principle of capacitively coupled contactless conductivity detection ($C^4D$), a capacitive-based contactless ET termed as the capacitively coupled electrical resistance tomography (CCERT) was proposed by Wang to address the problem of direct contact between the electrodes and the testing medium [16]. This new kind of capacitive-based electrical tomography (ET) is developed to reconstruct the conductivity distribution within the sensing area through the boundary resistance measurements collected by the electric capacitance tomography (ECT) sensors. The work conducted by Jiang [17] firstly introduced the CCERT for general biomedical application. In addition, CCERT has been further researched regarding to the brain imaging [18] and breast cancer detection [19]. Having the ability to reconstruct the conductivity spectra at a wide frequency range, CCERT is suggested to provide better discriminations between the different biological materials.

CCERT-related studies for medical applications so far mainly focus on the conductivity reconstruction [17-20]. In 2016, the Complex-Valued, Multi-Frequency Electrical Capacitance Tomography (CVMF-ECT) came up by Zhang reconstructed the permittivity and conductivity through the boundary complex admittance measurements in a simulated ECT sensor system for industrial application [21]. In addition, the capacitively coupled phase-based tomography provides a novel idea to demonstrate the complex dielectric parameter variation with phase measurement data [22]. With these applications as reference, the studies of capacitive-based electrical tomography for biomedical applications can also be extended to cover both the conductivity and permittivity reconstruction, forming the Cole-Cole load within a wide frequency range.

In this work, the multi-frequency capacitively coupled electrical tomography, reconstructing both the real and the reactive component of the effective admittivity, is studied for bio-tissue detection and characterization through both the resistance data and phase data. With an 8-electrode sensor system, several vegetables simulating different human bio-tissues were tested within the sensing region at the frequencies from 320 kHz to 14 MHz. The forward model is created based on a 3D ECT sensor model, which is meshed by the finite element method (FEM). To tackle the ill-posed problem of inverse problem, the spatial-spectral total variation (TV) reconstruction algorithm is applied. Both the reconstructed images and the Cole-Cole plot of the complex dielectric properties for different biomaterials are presented in the result section, showing the promising potential of this capacitive-based ET in the tissue characterisation with the reconstructed macroscopic tissue admittivity.

## II. BIO-IMPEDANCE

The electrical characteristics of biological tissues can be classified into active and passive ones based on the type of the electrical signal source. The closed structure of the cell is formed due to the existence of the cell membrane. The cell membrane which has the characteristics of semipermeable is composed of various proteins, glycolipids, and a bilayer of phospholipids. It controls the exchange of materials and ion movements inside and outside the cell. The charged molecules and ions partitioned at the different sides of the membrane will give rise of the electrical potential difference [23]. The electrical signal generated by the movement of the charged ions and particles is regarded as the active response. While when an external electrical field is applied, the response presented by the cells and bio-tissues is called the passive response, which can be quantitatively represented by bio-impedance.

Bio-impedance measurement is a non-invasive technique for biological tissue characterisation. When an external electric signal is given to the bio-tissue, the conduction of the current through the tissue is determined by its structure and composition, e.g., the cellular structure and density, ion concentrations in extracellular fluids (ECF) and intracellular fluids (ICF), molecular compositions, membrane characteristics, and other factors. In addition, the dielectric properties of bio-tissues show the frequency-dependent characteristic, which involves the interaction of the electromagnetic radiation and the constituents of bio-tissues at the cellular level [24].

The dielectric properties of tissues can be represented in terms of its complex permittivity $\varepsilon^*$:

$$\varepsilon^* = \varepsilon' - j\varepsilon'' \qquad (1)$$

$\varepsilon'$ is the relative permittivity, and $\varepsilon''$ is the out-of-phase loss factor that has the association with the total conductivity $\sigma$:

$$\varepsilon'' = \frac{\sigma}{\omega\varepsilon_0} \qquad (2)$$

where $\omega$ is the angular frequency of the electromagnetic field and $\varepsilon_0$ is the permittivity of free space. Therefore, the dielectric properties of tissues are determined by the relative permittivity $\varepsilon'$ and the conductivity $\sigma$. Equation (1) can also be written in the form of the effective admittivity $\gamma$:

$$\gamma = \sigma + j\omega\varepsilon_0\varepsilon' \qquad (3)$$

In a wide frequency domain, the increase of the conductivity and the decrease of the relative permittivity over the frequency have been reported in the literature [25]. Three main dispersions
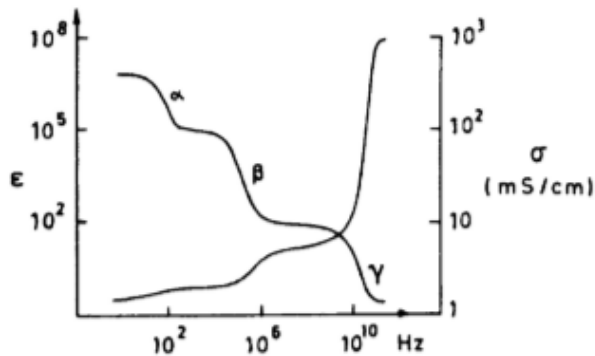
Fig. 1. Permittivity and conductivity variation of biological materials in the frequency domain (taken from [26]).

TABLE I
DIELECTRIC DISPERSIONS OF BIOLOGICAL MATERIALS.

| Dispersion | Operating Frequency Range | Feature |
|---|---|---|
| α-dispersion | Hundreds of hertz | This dispersion is associated with the ionic diffusion process at the cellular membrane. |
| β-dispersion | Hundreds of kilohertz | This dispersion is mainly caused by the polarization of membranes |
| γ-dispersion | Gigahertz | This dispersion is related to the polarization of water molecules. |

can be characterised for the dielectric spectrum, where each dispersion is associated with the particularly cellular mechanism. Figure 1 illustrates the spectrum of conductivity and permittivity for bio-tissues, Table 1 further details the operating frequency and the feature for each dispersion [24].

Among these dispersion steps, β-dispersion is mainly studied for bio-tissue characterisation with capacitive-based ET. The reason for that is the polarization of membrane happens over the frequency range of β-dispersion. Under such condition, the current passes only the external area of cell when the electric signal is applied at low frequency, as the capacitive membrane presents a high resistance. With the increase of frequency, the signal gradually crosses the membrane, passing both the ECF and ICF. Therefore, the overall conductivity of the sample is increasing along with the frequency. Figure 2 shows the conducting path of current in the bio-tissues at different frequency. According to the Cole models in β-dispersion range [27], the electrical equivalent circuit of the bio-tissues can be
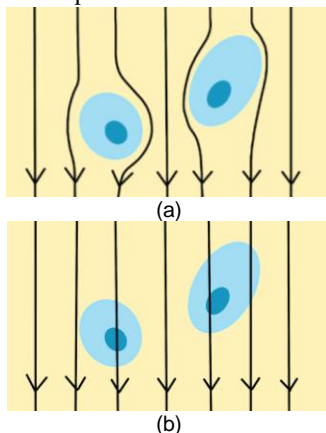


Fig. 2. Conduction path of current signal in Bio-tissues at (a) low frequency and (b) high frequency.
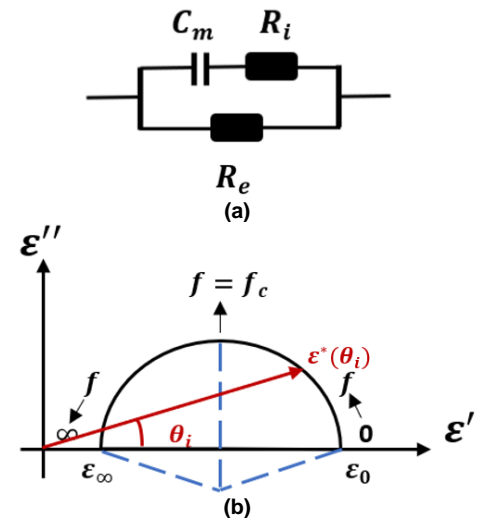


Fig. 3. (a) Fricke's equivalent circuit. (b) Dielectric Cole-Cole plot.

represented by Fricke's Cole-Cole model which is shown in Figure 3(a) [28], where $C_m$ is the equivalent capacitor of the membrane, $R_i$ and $R_e$ are the equivalent resistor of ICF and ECF, respectively. In addition, it's a popular way to demonstrate the complex impedance / admittance variation among the frequency domain with the Cole-Cole diagram plotted.

Cole-Cole diagram is the classical plot of the complex bioelectrical impedance/admittance spectroscopy. It demonstrates the variation of the bioelectrical impedance/admittance accompanied by the resistive and reactive components along with the frequency [8]. In a Cole-Cole model, the overall complex impedance / admittance forms a circular arc with the change of frequency [29-30]. In Figure 3(b), the Cole-Cole diagram of the complex dielectric parameter is shown. The blue dash shows the radius of the circular arc which starts from $\varepsilon_0$ to $\varepsilon_\infty$, and passes $\varepsilon_{f_c}$ in the middle. $\varepsilon_0$ and $\varepsilon_\infty$ is the complex permittivity at the zero and infinite frequency, respectively. $f_c$ is the characteristic frequency, at which the imaginary part of the complex permittivity is at maximum [31-32]. Here, an example point $\varepsilon^*(\theta_i)$ is also shown, it is the complex permittivity at the frequency $\theta_i$.

## III. METHOD

Capacitively coupled electrical tomography (CCET) is a tomographic technique capable of imaging the complex permittivity distribution within the ROI. The fundamentals of CCET is based on the principle of Conservation of Electromagnetic Energy in the sensing region. By injecting an AC electrical signal to a set of electrode-array, a time-varying electromagnetic field can be established. When the distribution of the internal electrical properties occurs changes, the electrical boundary measurements will then consequently appear a changing value. Based on the analysis of boundary measurement difference, various electrical parameters can be reconstructed with the forward model and the reconstruction algorithm.

### A. System Architecture and Measurement Principle

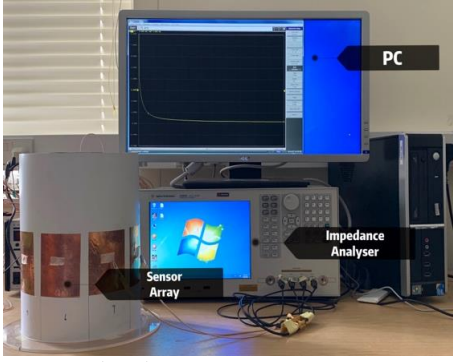The whole system of the proposed imaging technique
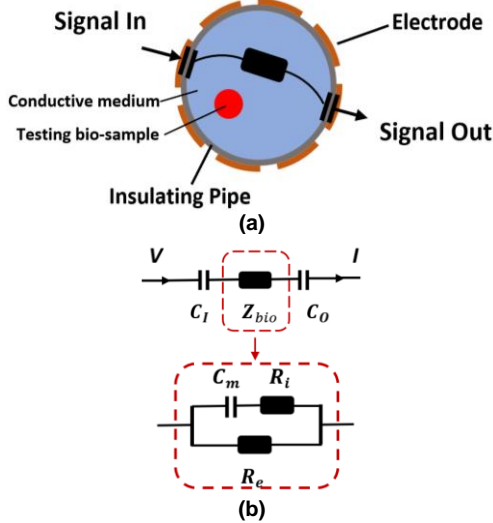
Fig. 4. Measurement system.



Fig. 5. (a) The 8-electrode single-layer sensor for cross-sectional (2D) image. (b) The equivalent circuit for one electrode pair during measurement. $C_I$ and $C_O$ are the equivalent capacitors formed by the electrodes, insulting material and the conductive medium. $Z_{bio}$ is the impedance of the conductive medium and the testing bio-sample, which can be represented by the Fricke's equivalent circuit.

comprises three parts: (i) a set of sensor array consisting of 8 cooper electrodes; (ii) the impedance analyser (IA) based data acquisition system; (iii) a host PC which is for data analysis and image reconstruction. A photograph of the measurement system and phantom used is shown in Figure 4.

Illustrated in Figure 5(a), the electrodes are equally spaced around the outer boundary of the insulating pipe. In the sensing region, the boundary resistance and phase measurements can be obtained with injecting the multi-frequency time-varying voltage to the electrodes. When the excitation signal is applied, the capacitor will be formed among the electrode, the insulating material and the conductive medium. Since the saline water is used to simulate the in vivo biochemical environment, this conductive medium can be treated as ECF when the bio-sample is placed inside the phantom. In this way, the equivalent circuit between one measuring electrode-pair can be represented as a series connection of two capacitors and one bio-impedance, Figure 5(b) plots the corresponding circuit.

The operation principle of the system is detailed as follows. At the first step, electrode 1 is selected as the transmitting sensor, electrode 2 to 8 are working as the receiving sensor in turn. Then, electrode 2 is the transmitter and electrode 3 to 8 are the receivers one by one. This process will be repeated until electrode 7 and 8 are the transmitting and receiving electrode. Thus, there is 28 ($L \times (L-1)/2$, $L=8$) independent measurement

data from complex admittance covering all electrode-pair will be collected during one measuring cycle.

## B. Image reconstruction

CCET being a model-based imaging technique, the process of reconstructing the images and admittivity parameters can be carried out in two steps, solving the forward problem and the inverse problem. The simulation of the measuring process, which termed as forward problem, will be firstly conducted to obtain the relationship between the given internal dielectric distribution and the simulated boundary measurements. After creating the sensitivity matrix that represents the link, the electrical properties within the ROI can be reconstructed from the experimental boundary electrical differences with the reconstructing algorithm, and this step is called the inverse problem. The imaging is usually carried out based on the time-difference method, where the admittance data are measured at two different times. The data measured at time $t_1$ is used as the background reference, and the other one measured at $t_2$ ($t_1 \neq t_2$) is treated as the changing measurement. With the multifrequency time-difference method, the variation of complex admittivity, with the background as the reference, over the frequency domain can be extracted.

The dynamic electromagnetic field for CCET system can be regarded as the quasi-static electromagnetic field because the excitation signal is normally at low frequency. For this reason, the general divergence of Maxwell-Ampere equation in the sensing region $\Omega$ can be written as:

$$\nabla \cdot \big(\sigma(x,y) + j\omega\varepsilon(x,y)\big)\nabla\phi(x,y) = 0 \qquad (4)$$

where $\sigma(x,y)$ and $\varepsilon(x,y)$ are the distributions of conductivity and permittivity. $\phi(x,y)$ is the electrical potential. $\omega$ is the angular frequency of excitation signal. Based on the driven pattern of excitation signal, the boundary conditions are represented as:

$$\begin{cases} \phi_m(x,y) = V_i \\ \phi_n(x,y) = 0 \\ \frac{\partial\phi_t(x,y)}{\partial\vec{n}} = 0 \end{cases} \qquad (5)$$

where $V_i$ is the amplitude of the excitation voltage signal. m and n are the index of transmitting and receiving electrode. t represents the floating electrode and $\vec{n}$ is the normal vector pointing out of the boundary.

The sensitivity matrix, that reflects the relationship between the complex dielectric properties and the boundary complex admittance measurements, is required in this work. With (4) as the basement, the sensitivity matrix is established with the adaptions of the complex capacitance system [20]. Therefore, the integral relation between the complex admittance $Y_{complex}$ and the distribution of conductivity and permittivity at the angular frequency $\omega$ can be represented as:

$$Y_{complex} = \frac{1}{V}\int (\sigma + j\omega\varepsilon_0\varepsilon')\nabla\phi \, d\Gamma$$
$$= \frac{j\omega}{V}\int \left(\varepsilon - j\frac{\sigma}{\omega}\right)\nabla\phi \, d\Gamma$$
$$= \frac{j\omega}{V}\int (\varepsilon^*)\nabla\phi \, d\Gamma \qquad (6)$$

$V$ is the potential difference of the electrode pair and $\Gamma$ is the surface of electrode. The conductance measurements denominate to the real part of the complex admittance, and the pure capacitance measurements contribute to the imaginary part
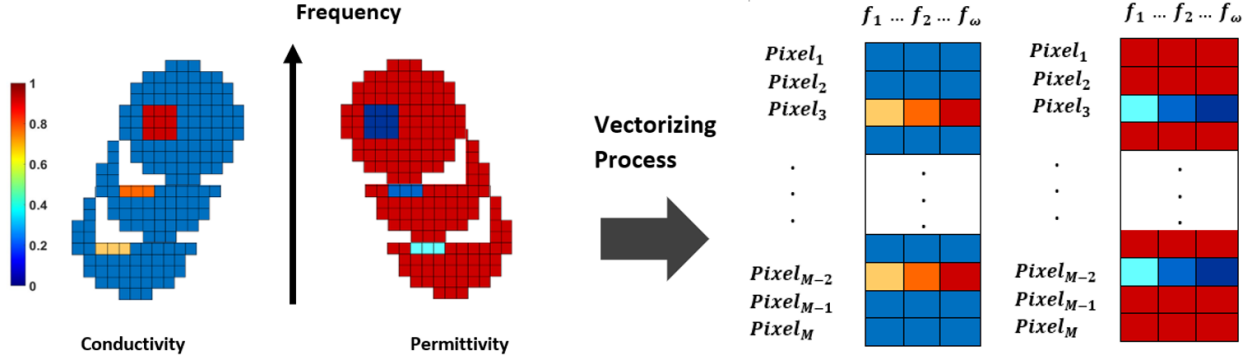
Fig. 6.  Frequency constraints of reconstructed conductivity and permittivity among pixels. (The demonstration diagram is adopted from [34])
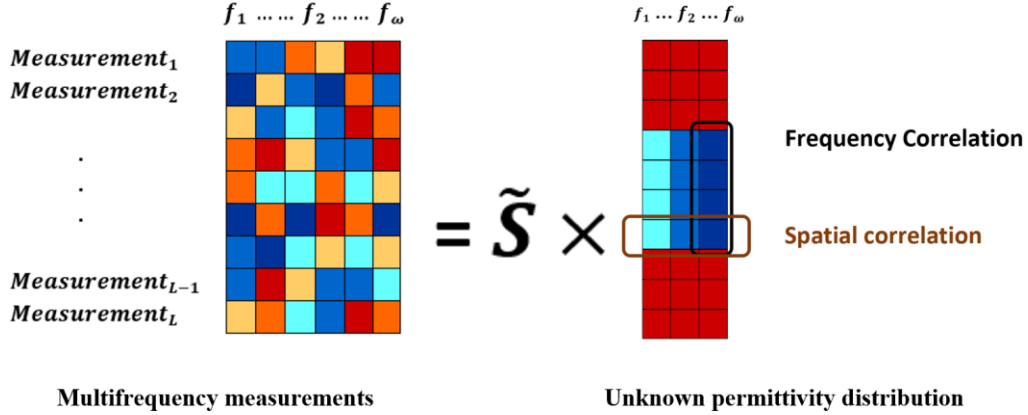


Fig. 7.  Spatial-spectral correlation reconstruction model. (permittivity is selected as demonstration, and the demonstration diagram is adopted from [34])

of the complex admittance. When there is a small disturbance happens to the dielectric distribution, the boundary complex measurement difference can be written as:

$$\Delta C_{co} = F(\Delta\sigma, \varepsilon, \omega),$$
$$\Delta C_{ca} = F(\Delta\varepsilon, \sigma, \omega) \quad (7)$$

where $F$ is the forward mapping from the dielectric property changes to boundary complex admittance measurement changes. $C_{co}$ is the conductance measurement and $C_{ca}$ is the capacitance measurement. As the common drawback of all types of electrical tomography is their soft-field characteristic, the forward model needs to be meshed into limited number of elements firstly, and the general approach is implementing the finite element method (FEM). After discretising both the sensing area and the electrodes, a linear relationship between the boundary measurements and the internal dielectric properties can be obtained, and (7) can be rewritten as follows:

$$\begin{bmatrix} \Delta C_o \\ \Delta C_a \end{bmatrix} = \begin{bmatrix} S_{co} & S_{ca} \end{bmatrix} \begin{bmatrix} \Delta\sigma \\ \Delta\varepsilon \end{bmatrix} \quad (8)$$

where $\Delta C_o \in \mathbb{R}^m$, $\Delta C_a \in \mathbb{R}^m$, $\Delta\sigma \in \mathbb{R}^n$, $\Delta\varepsilon \in \mathbb{R}^n$, $S_{co} \in \mathbb{R}^{m \times n}$, and $S_{ca} \in \mathbb{R}^{m \times n}$. Based on the reciprocity theorem [33], $S_{co}$ and $S_{ca}$ can be calculated for each excitation frequency as:

$$\begin{cases} S_{co}(\omega) = -\int_\Omega E_1(\frac{\sigma}{\omega}) \cdot E_2(\frac{\sigma}{\omega}) dV \\ S_{ca}(\omega) = -\int_\Omega E_1(\varepsilon) \cdot E_2(\varepsilon) dV \end{cases} \quad (9)$$

With the sensitivity matrix, (8) can be simplified as:

$$\Delta Y^* = S\Delta\varepsilon^* \quad (10)$$

For the inverse problem, the principle of image reconstruction by CCET is to retrieve the unknown complex permittivity $\varepsilon^*$ distribution with the sensitivity matrix $S$ and the complex admittance projection vector $Y^*$. The conventional method is solving the least-square problem. Though the common practice is to do calculations for each frame independently, this approach is not optimal as the redundant information from the previous calculation will be repeatedly used. In order to avoid the redundant information, the least-square problem can be written as:

$$\underset{\Delta\varepsilon_f^*}{arg\,min}\ \phi(\Delta\varepsilon_f^*)$$
$$s.t.\ \left\|S\Delta\varepsilon_f^* - \Delta Y_f^*\right\|_2^2 < \delta,\ \forall f = 1, \dots, \omega_n \quad (11)$$

where $\phi(\Delta\varepsilon_f^*)$ is the convex regularization function which carries the prior information of the unknown complex permittivity, and $\omega_n$ is the total number of spectral frames. The unknown complex permittivity and the boundary complex admittance are both multi-dimensional data.

Since the challenge for all soft-field imaging modalities including CCET is the ill-posed problem, the regularization term needs to be added to (11). In this paper, the spatial-spectral total variation (TV) regularization method is applied with an augmented Jacobian $\tilde{S}$:

$$arg\,\underset{\Delta\varepsilon^*}{min}\left\|\nabla_{x,y,z}\Delta\varepsilon^*\right\|_1 + \left\|\nabla_\omega\Delta\varepsilon^*\right\|_1$$
$$s.t.\ \left\|\tilde{S}\Delta\varepsilon^* - \Delta Y^*\right\|_2^2 < \delta \quad (12)$$

The first and second term in (12) correspond to the spatial TV and spectral TV, respectively. The augmented Jacobian $\tilde{S}$ works on the frame-by-frame basis. As shown in Figure 6, the reconstructed conductivity and permittivity data at the same frequency for all pixels are stored in one column, and the data

for the same pixel with the multi-frequency are stored in one row. Based on such frequency constraints, the spatial-spectral correlation reconstruction model shown in Figure 7 is used to avoid the redundant information. In order to effectively solve the constrained problem, the Bregman iteration is used in this work to convert the constrained problem (11) to an iterative scheme [35]:

$$\Delta\varepsilon^{*k+1} = arg\ \min_{\Delta\varepsilon^*} \left\|\nabla_{x,y,z}\Delta\varepsilon^*\right\|_1 + \left\|\nabla_\omega\Delta\varepsilon^*\right\|_1 +$$

$$\sum_{i=1}^{\omega_n}\frac{1}{2}\left\|\tilde{S}\Delta\varepsilon^* - \Delta Y^{*k}\right\|_2^2 \qquad (13)$$

$$\Delta Y^{*k+1} = \Delta Y^{*k} - \tilde{S}\Delta\varepsilon^{*k+1} + \Delta Y^* \qquad (14)$$

As the L1-norm function has the non-differentiability characteristic, the split Bregman method is applied to extend the minimisations of the L1-norm regularization terms [36], where the L1- and L2- functions can be solved in separate steps. With the splitting technique, (13) can be rewritten as:

$$\left(\Delta\varepsilon^{*k+1}, d_x, d_y, d_z, d_\omega\right) =$$

$$arg\ \min_{\Delta\varepsilon^*, d_x, d_y, d_z, d_\omega} \left\|d_x, d_y, d_z\right\|_1 + \left\|d_\omega\right\|_1 +$$

$$\frac{1}{2}\left\|\tilde{S}\Delta\varepsilon^* - \Delta Y^{*k}\right\|_2^2 \qquad (15)$$

and

$$d_x = \nabla_x\Delta\varepsilon^*, d_y = \nabla_y\Delta\varepsilon^*, d_z = \nabla_z\Delta\varepsilon^*,$$

$$d_\omega = \nabla_\omega\Delta\varepsilon^* \qquad (16)$$

The algorithm will produce the image of complex admittivity in spectral correlative fashion. As we will see in following section measured data, it is not straight forward to select the image reconstruction parameters that produces sharp images for real and imaginary parts in all these very wide range frequencies. In such a spectral complex imaging the focus remains producing the complex admittivity plots in each pixel (or more practically in each region) within the imaging domain. Here we selected image regularisation empirically, an automatic selection of image reconstruction parameter will be subject of a future theoretical and computational studies.

## IV. EXPERIMENTAL RESULTS

In this section, the laboratory phantom tests of multi-frequency CCET are demonstrated for several different scenarios. To investigate the ability of CCET for tissue characterisations, the experiments can be classified into two groups. The first group is the study of the single inclusion material characterisation, and the second one is the investigation of double inclusions test, including the double-phase and triple-phase difference. The multi-frequency reconstructed admittivities are represented in the format of reconstructed images, spectral profiles, and the Cole-Cole diagram produced with the reconstructed data.

### A. Experiment setup

Illustrated in Figure 4, an 8-electrode CCET system operating at frequencies from 320 kHz to 14 MHz was tested for biological materials characterisation. 342 frequency sample points were selected among the frequency range with the equal 40 kHz frequency gap. The cooper electrodes with the same size 65mm × 100mm are equally spaced around the outside of a cylindrical plastic tank. The size of this plastic phantom is 300mm height and 200mm outer diameter, and the thickness of its wall is 3mm. During the measurement, the data is acquired by the Keysight 4990A Impedance Analyser (IA) under the condition of 1V Peak to Peak excitation AC voltage signal. For each complete measuring cycle, 28 independent data will be collected.

The testing biological materials are potato and carrot, which represent the cancerous and normal tissues of human body, respectively. 0.9% saline water is used as the conductive background medium, simulating the in-vivo chemical environment. The experimental temperature maintained 25 ℃ during the test.

### B. CCEIS for single sample characterisation

The main motivation behind this work was to show the applicability of CCET for diagnosing the lesion or cancerous tissue within the target area through the regional electrical properties' reconstruction. Therefore, references can be provided for future clinical applications through the investigation of CCET in discriminating different biological materials.

During the investigation of CCET, the first conducted experiment is about the single inclusion characterisation. It should be noted that, compared with the traditional EIT, CCET also has the soft field characteristic. Therefore, the sensitivity near to the sensing boundary is higher than that at the centre area. The soft field characteristic brings challenges for solving the inverse problem, while the optimised regularization algorithm and the fast-developed machine learning may ease the difficulties in image reconstruction. In this work, the improvement of inverse problem will not be explained that much, as the application of CCET for characterising different biomaterials is mainly focused. Therefore, the testing inclusion was only placed at the location that is near to the sensor. During the test, the biological samples, which is potato and carrot, were cut into the same size as 300 mm height and 40 mm base diameter.

Before starting the main control experiments, we measured the background data when there was only saline water inside the phantom. Following this step, the single potato sample was firstly placed near to the edge of the sensing region and tested.



(a)                                                                          (b)

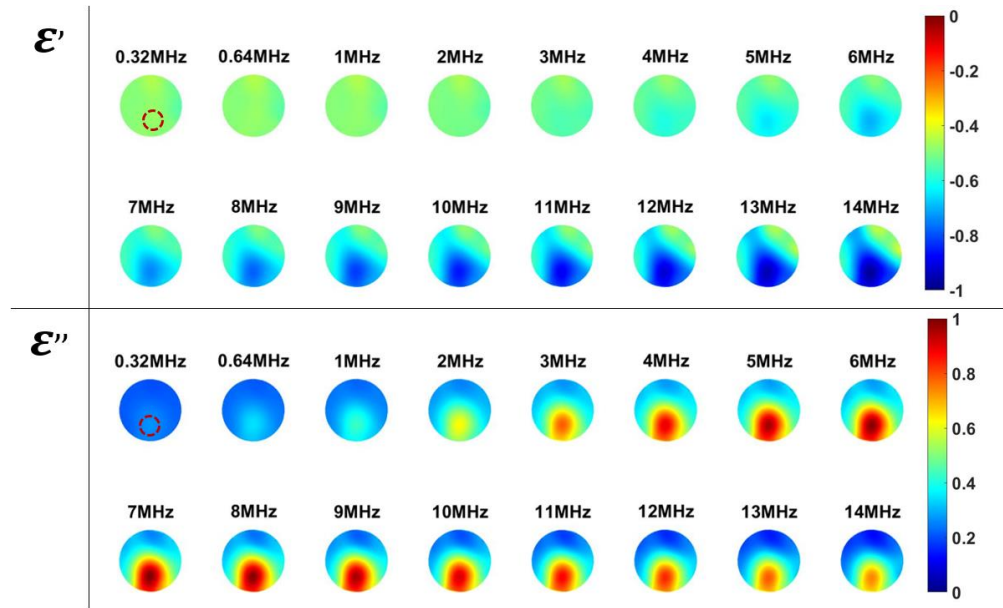Fig. 8.  Experiment scenario for single inclusion characterisation.

Fig. 9. The reconstruction of complex permittivity for single potato sample characterisation with the multi-frequency ranging from 320 kHz-14 MHz.
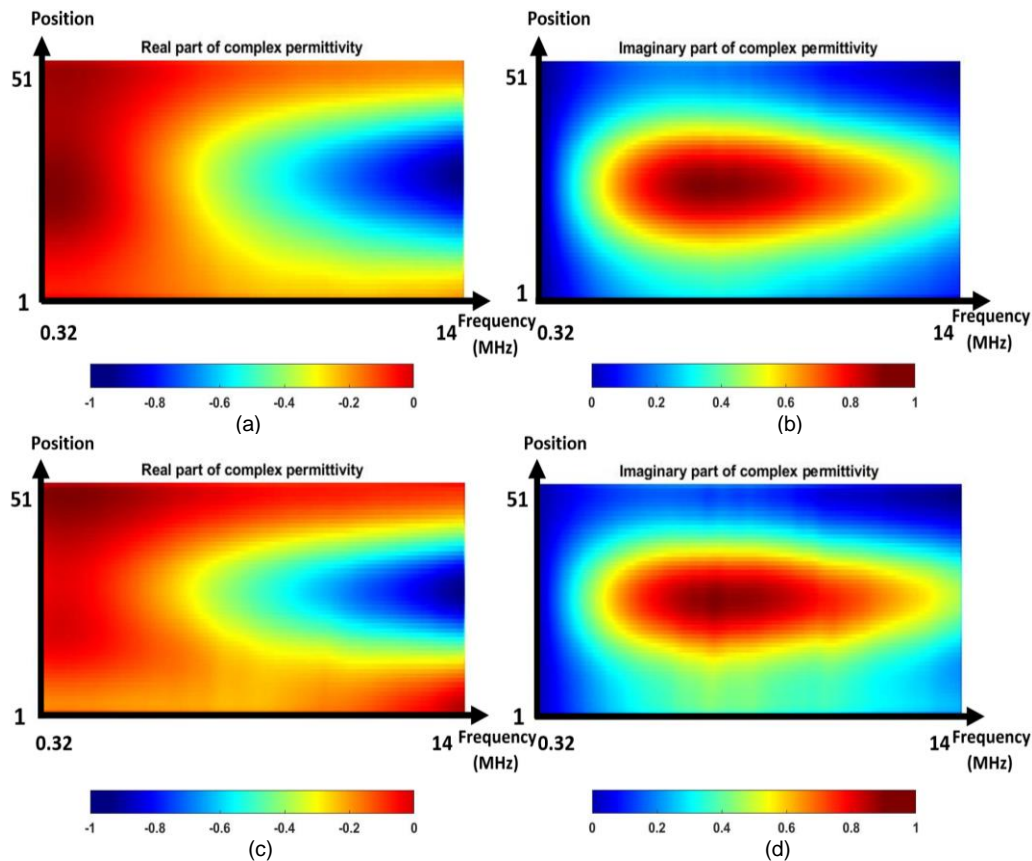


Fig. 10. Spectral profile for potato sample ((a) $\varepsilon'$ (b) $\varepsilon''$). and carrot sample ((c) $\varepsilon'$ (d) $\varepsilon''$). Frequency range demonstrated here is 320 kHz-14 MHz.

After collecting the measurement data of potato, the test for single carrot sample was repeated at the same position. Figure 8 shows the experiment scenario.

Illustrated in Figure 9, the reconstructed complex permittivity of potato sample, standing at the location shown in Figure 8 (a), presents the reasonable change at the frequency ranging from 320 kHz to 14 MHz. The images in one group are regularized into the same colorbar scale. After repeating the analysis of carrot, the spectral profiles of potato and carrot are compared in Figure 10, where the variation of complex
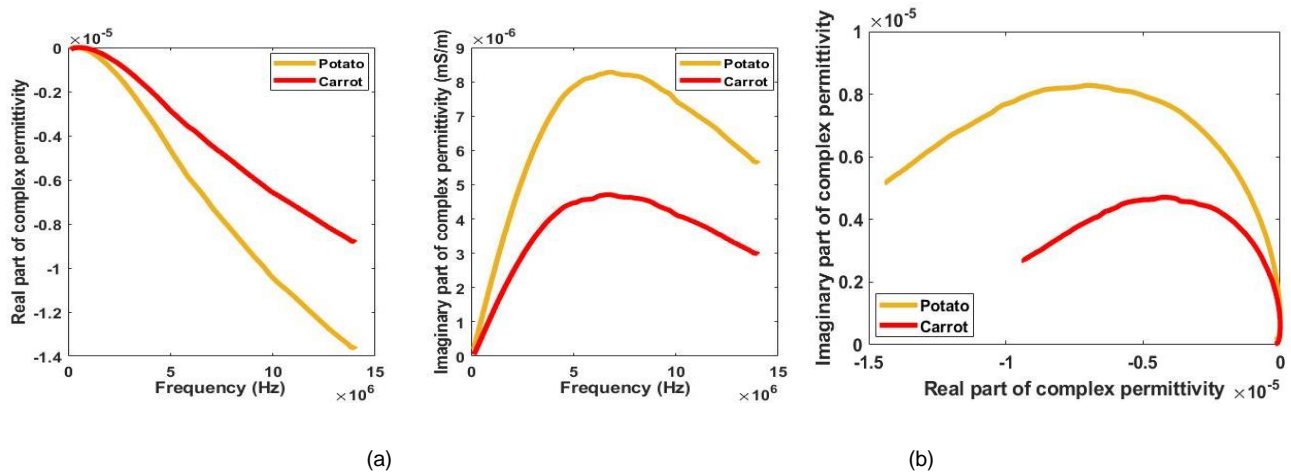
(a)                       (b)

Fig. 11. (a) Reconstructed complex permittivity spectra for potato and carrot sample at frequency from 320 kHz to 14 MHz. (Left image is $\varepsilon'$ plot and right one is $\varepsilon''$ plot).(b) Cole-cole plot of data extracted from the reconstructed images for different biomaterial with multi-frequency CCET system.

permittivity with respect to the frequency for single biomaterial is demonstrated. The vertical axis represents the spatial longitudinal-section that passes through sensor 3 and sensor 7, and position 1 to 51 is the number of pixels for the longitudinal-section. The horizontal axis represents the frequency domain from 320 kHz to 14 MHz. From the profiles, it can be observed that the $\varepsilon'$ and $\varepsilon''$ for different bio-samples have the similar variation tendency in the frequency domain, where with the conductive saline water as the background, the $\varepsilon'$ decreases along with the frequency while $\varepsilon''$ increases firstly and then drops. But through the comparison, the different change rate of complex permittivity for potato and carrot sample is noticeable. In Figure 11 (a), the spectra of permittivity and conductivity/frequency values are shown. The values of these spectra are calculated by averaging the reconstructed complex permittivity within the target region. Assuming that the ratio of the cross-section area of the testing sample to the entire ROI is $R_{area}$. In this work, the testing samples were cut into cylinders for primary investigation. Then the target region is an area centred at the extremes of the reconstructed target with a certain length as radius, and the ratio of the target region to the entire reconstruction image size also equals to $R_{area}$. Take the potato sample as an example, the $R_{area}$ can be calculated as $\frac{\pi(20mm)^2}{\pi(100mm)^2} = 0.04$. As the size of the reconstructed 2D image is 2601 ($51 \times 51$) pixels, the target region should be the area covering around 104 pixels and centred at the point that has the extreme value. The target region for the other shape of the testing sample should be defined according to their cross-section region with the similar method. At the same frequency, the potato sample has a lower permittivity while a higher conductivity compared with the carrot sample. In the Cole-Cole plot of the complex permittivity values, the characteristic frequency ($f_c$) of potato sample is higher than that of carrot.

## C. CCEIS for multiple samples characterisation

In the second set of experiments, we explored the ability of CCET in detecting multi-inclusions within the sensing area. The testing samples were placed on the opposite sides in the same horizontal direction. Before conducting the double inclusions test, we did an extra exam by using a single potato sample which stood at the each of these two opposing points separately. The aim of this extra experiment is to test whether the electrical signals obtained when sample locates at these two opposing points are the same, ensuring that the errors are within the reasonable limits when the double inclusions test are carried out. Hence the Cole-Cole diagram of the two different samples can be guaranteed to be meaningful. Besides, it's also a good investigation for the testing samples' location detection.

The potato sample was cut into the size around 200 mm height and 40 mm bottom side length, placed on a plastic holder. The height of the holder is smaller than the distance between the near bottom side of the electrode and the phantom bottom, so the excitation signal will not be affected by the plastic holder. With the measured resistance and phase data, the variation of the real ($\varepsilon'$) and imaginary ($\varepsilon''$) part of the complex permittivity for potato at different location can be reconstructed in the frequency domain.

In the time difference imaging approach, the changes in the real part and imaginary part of the complex permittivity for single potato sample according to the true position were detected, showing the reasonable spectra variation in the wide frequency domain (320 kHz – 14 MHz). The true position of the inclusion is marked by a red circle in the first image of each group. With the conductive saline water as the background, the effective permittivity ($\varepsilon'$) for potato sample keeps decreasing while its loss factor ($\frac{\sigma}{\omega}$) increases firstly and then decreases. In Figure 16, the Cole-Cole diagrams of the data extracted from the reconstruction images are compared for potato standing at different locations. Though we tried to keep the distance between the sample and the nearest wall maintain the same during the test, the sample standing at the right side of the phantom has a slightly smaller distance to the nearest wall. Therefore, the sample located at the right side presented a slightly different value Cole-Cole diagram compared to the one obtained when it is at the left side, but the overall arcs show a high similarity with the similar value range of both real and imaginary part of the complex permittivity.

As the measurements collected at these two locations show similar results, we continued the test of CCET in detecting multi-inclusions within the sensing area. The testing samples are still potato and carrot. In order to minimize the interference between the samples when there is more than one sample inside

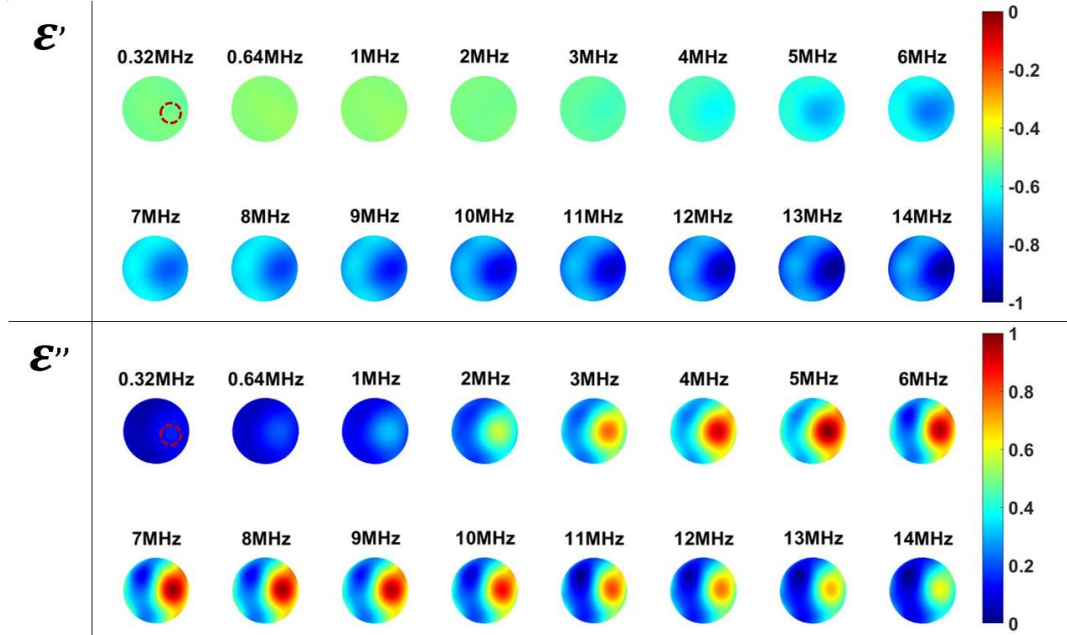Fig. 12.  The experiment scenario for location detection.



Fig. 13.  The reconstruction of complex permittivity for potato standing at the right side of the phantom with the multi-frequency ranging from 320 kHz-14 MHz.



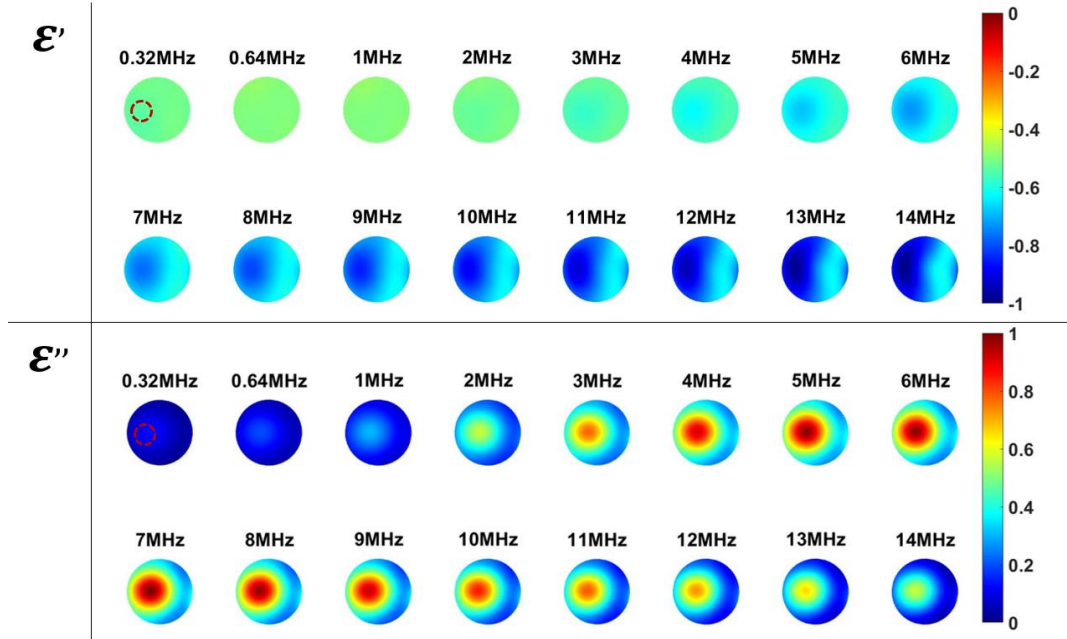Fig. 14. The reconstruction of complex permittivity for potato standing at the left side of the phantom with the multi-frequency ranging from 320 kHz-14 MHz.

the phantom, the bottom side length of the samples in this test is reduced to half. The size of the sample is 200 mm height and 20 mm bottom side length/bottom diameter. And the frequency is ranging from 320 kHz to 10 MHz. During the measuring
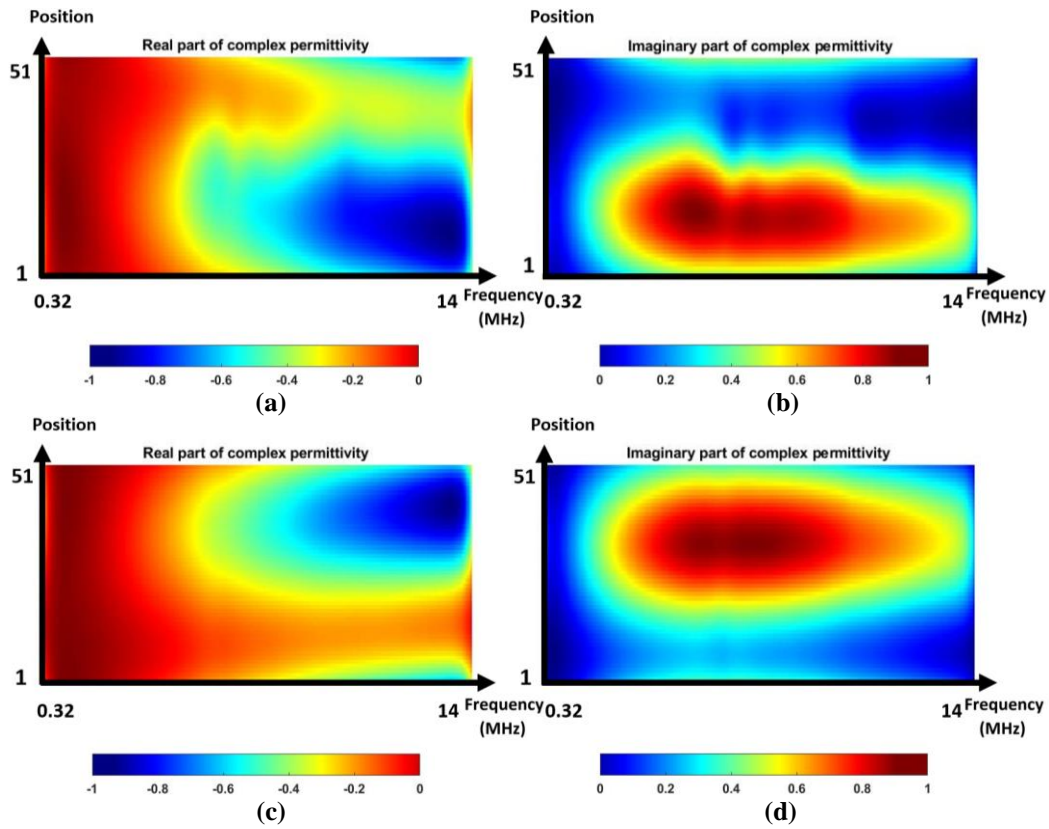
Fig. 15. Spectral profile for single potato sample standing at the right side of the phantom ((a) $\varepsilon'$ (b) $\varepsilon''$) and left side of the phantom ((c) $\varepsilon'$ (d) $\varepsilon''$). Frequency range demonstrated here is 320 kHz-14 MHz.
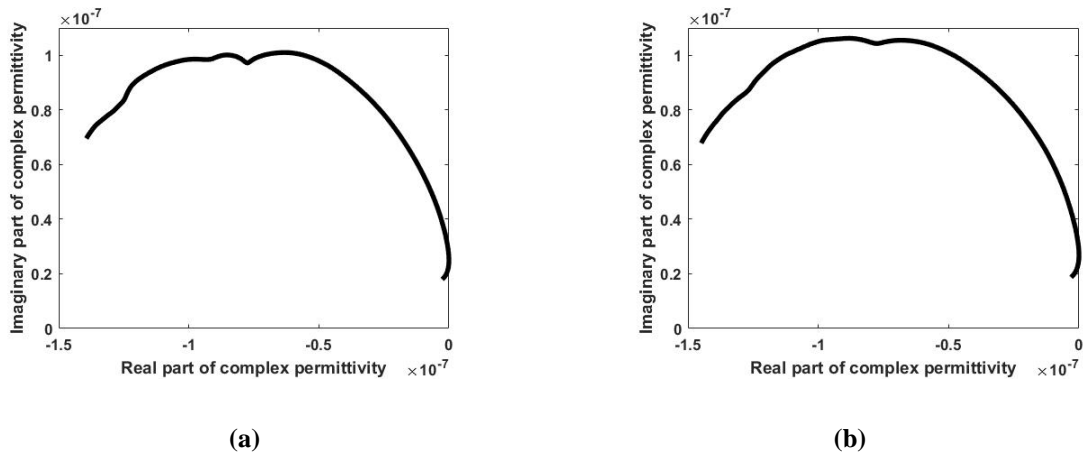


Fig. 16. Cole-Cole plot of data extracted from the reconstructed images for potato sample standing at (a) right side of phantom (b) left side of phantom

process, the smaller potato sample was firstly located at the right side of the sensing area near to the boundary, then the carrot sample was placed on the opposite site of the potato for the double inclusion detection. The experimental setup is shown in the Figure 17. Figure 18 and Figure 20 shows the reconstructed complex permittivity. The Cole-Cole diagram of the complex permittivity value which is extracted from the image can be compared in Figure 19 and Figure 22 for these two biomaterials.

From the reconstructed images shown in Figure 20 and 21, CCET has the ability to detect multiple inclusions according to

their accurate location. But more importantly, the Cole-Cole diagram which is composed of the data obtained from the CCET reconstructed images can more intuitively characterize different materials. When both potato and carrot sample were inside the phantom, the conductivity of potato is bigger while the permittivity is smaller than those of carrot at the same frequency. These findings match with the results demonstrated in section IV-B. But compared to the experiments in the section IV-B where different samples were measured separately, the centre frequencies of potato and carrot are relatively closer in this section. In addition, when compared the Cole-Cole

(a)                                                                                                                 (b)
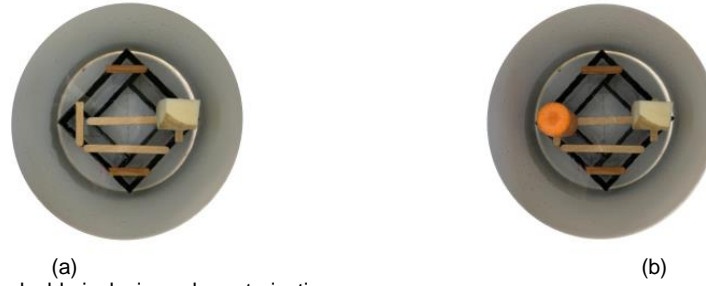
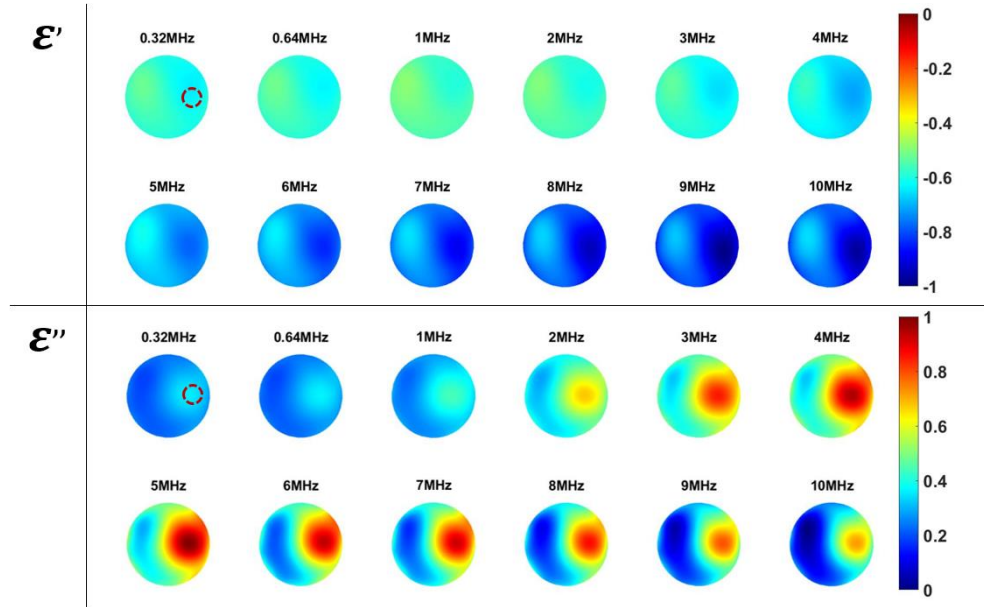Fig. 17.  Experiment scenario for double inclusions characterisation.



Fig. 18.  The reconstruction of complex permittivity for small potato sample with the multi-frequency ranging from 320 KHz-10MHz.
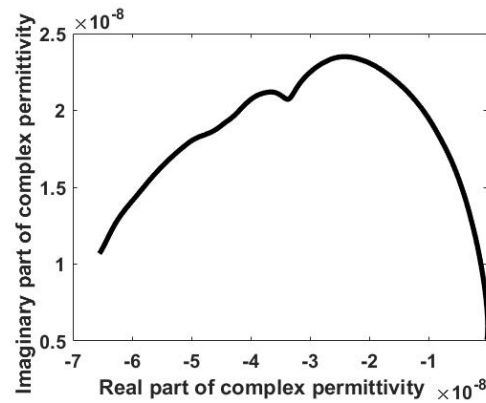


Fig. 19.  Cole-Cole plot of data extracted from the reconstructed images for single small potato sample with multi-frequency CCET system

diagrams in Figure 19 and Figure 22, it should be noted that the absolute value of the real and imaginary parts of the complex permittivity for potato sample is larger at the double inclusions test than that obtained at the single inclusion test. These results are reasonable as the target object will be affected by its surroundings due to the soft-field characteristic. In the future research, the interference between different materials can be reduced by optimizing the reconstruction algorithm.

Regarding the sample recognition, the different samples were tested separately in section IV-B but together in section IV-C, and the size of the samples is larger in the former than the samples used in the latter. Through the comparison between the results shown in Figure 11 and Figure 22, the differences can be found in their arcs, and the reasons of the difference can be explained in two aspects. The first one could be when the different samples are measured together in the phantom, the
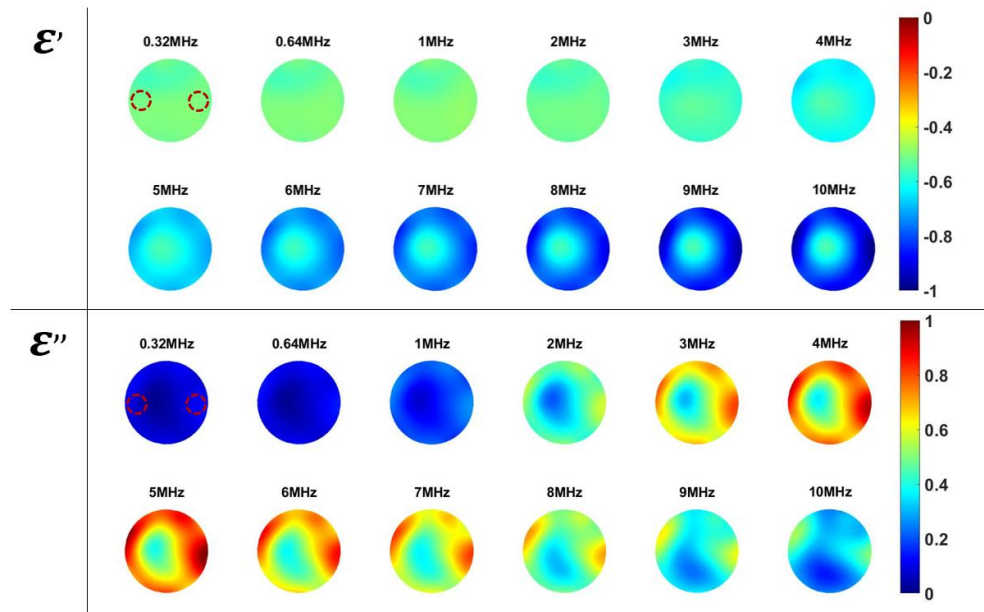
Fig. 20.  The reconstruction images of complex permittivity for double inclusions test, small potato and carrot sample, with the multi-frequency ranging from 320 KHz-10MHz.



(a)                                                                                                (b)
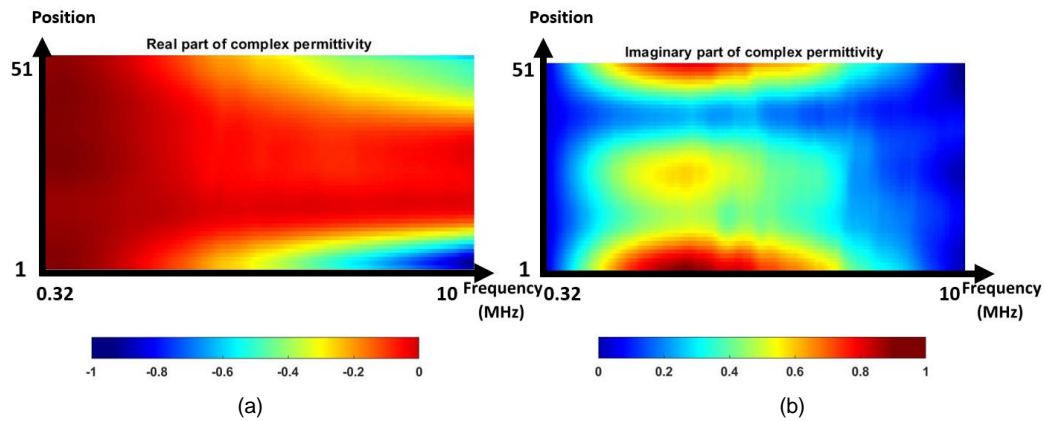
Fig. 21. Spectral profile (a) $\boldsymbol{\varepsilon'}$ (b) $\boldsymbol{\varepsilon''}$ for multi samples (Reconstructed object near to the Position 1 is potato, near to the Position 51 is carrot.)



(a)                                                                                                (b)
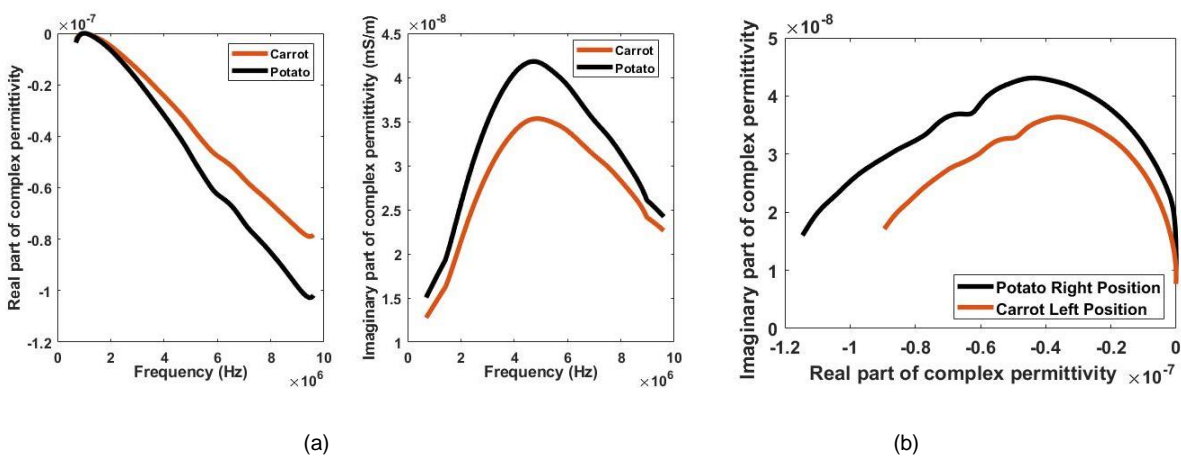
Fig. 22.  (a) Reconstructed complex permittivity spectra for double inclusions test, small potato and carrot sample, at frequency from 320 kHz to 10 MHz. (Left image is $\varepsilon'$ plot and right one is $\varepsilon''$ plot). (b) Cole-cole plot of data extracted from the reconstructed images for double inclusions: small potato and carrot, with multi-frequency CCET system.

signals between the samples will partially merge and interact each other, thus, the difference in reconstructed electrical properties between different samples will reduce. The second reason could be the influence brought by size. When the sample

has a smaller size, the signal strength is correspondingly weakened, so it will be easier to be affected by the noise, such as the parasitic capacitance in the cables, and the interaction of surrounding electromagnetic field. Consequently, the accuracy of reconstruction algorithm and system optimization are demanding in the future work. But judging from the results presented in this work, CCET still shows its ability in identifying different bio-samples.

Overall, through the experimental verification on biological samples, the investigation of multi-frequency CCET for bio-tissue characterisation by reconstructing the regional admittivity has been conducted. The experiments have shown that CCET is able to detect and discriminate between different bio-samples in a wide frequency range (several kHz - several MHz). The electrical spectrum of biological tissues can be reconstructed and analysed by reconstructing images with Cole-Cole plots. Through the theoretical analysis and experimental validation, multi-frequency CEIT could be applied to diagnose cancer and monitor stroke in the future. There are greater differences in electrical properties between tumours and normal tissues in cancer imaging in higher frequency range. For stroke, the electrical properties of local tissues will also change significantly. Strokes are classified into haemorrhagic and ischaemic strokes, where haemorrhagic stroke is caused by the rupture of the blood vessels, while ischaemic stroke is caused by the blockage of the blood vessels. The relevant literature shows that, between several kHz to 1MHz, the conductivity of blood is higher than that of ischemic tissues, and the variation in the relative permittivity of blood is also greater than that of ischemic tissues [37]. Although there are relatively few studies on changes in electrical properties in ischaemic tissue above 1MHz, there are lots of studies showing that the significant changes in conductivity and permittivity of blood can be noticed with excitation frequencies above 1MHz, so the use of excitation signals with multifrequency among several kHz to several MHz has positive implications for post-treatment monitoring of stroke. So far, direct contact electrode EIT has been studied for stroke detection, but it focuses mainly on conductivity variations. The low conductivity of skull brings the challenge to contact based EIT for brain imaging, but the promising results reveal the potential of CCET as it performs well in higher frequencies. In this work, the two different biomaterials used for experiments can also be regarded as the simulation of two types of stroke. Therefore, in the future, CCET can be further studied to reconstruct the Cole-Cole plot to give the whole picture of the area of interests in the case of stroke. As an assistant to CT and MRI, CCET has the potential to be an alternative for rehabilitation and damage monitoring of stroke during treatment and recovery.

## V. DISCUSSION AND CONCLUSION.

In this work, the study of multi-frequency CCET for characterizing different biological samples through reconstructing the complex permittivity was conducted. The previous medical-related applications of CCET mainly focused on the variations of bioelectrical conductivity in the frequency domain. However, based on the fact that cells will undergo different polarizations under the multifrequency excitation signal, the changes in permittivity are equally important indicators as the changes in conductivity in the application of tissue characterization. Therefore, studying both the conductivity and permittivity spectra at the same time will allow us to better understand the bioelectrical properties' behaving in frequency domain, and further provide better discrimination of different bio-tissues with CCET.

The mathematical model of CCET was established by referring to the model of CV-ECT, and the total variation (TV) regularization term was applied to ease the ill-posed problem in image reconstruction. Regarding the experiments, different bio-samples were used to simulate the cancerous and normal tissue. As the knowledge of CCET for medical imaging is limited, it is essential to conduct the lab-based experiments before the clinical use. With the 1V excitation voltage signal applied at frequency ranging from 320 kHz to 14 MHz, the tests of single-inclusion characterisation, and double inclusions characterisation were carried out step by step. From the experimental results, the proposed imaging technique has successfully identified and distinguished different bio-samples. The Cole-Cole diagram of the reconstructed complex permittivity also shows how the two characteristics of it change in that wide frequency range. Though the research on CCET for medical imaging application so far is at a relatively preliminary stage, the experiments carried out in the tank phantom validate the detecting ability of CCET. With the enhance TV algorithm, it's possible to have the reconstructed image with a sharp boundary, clearly showing the shape and the size of the testing inclusion, however, producing the very sharp image can result in losing the quantitative regional information. Thus, the trade-off between the clear boundary image and the quantitative regional information needs to be made during the analysis. For this work, it's valuable to analyse the regional information presented in the Cole-Cole diagram format. And the information brought by the results can be useful reference for future clinical approach.

## REFERENCES

[1] M. Schwarz, M. Jendrusch and I. Constantinou, "Spatially resolved electrical impedance methods for cell and particle characterization," *Electrophoresis*, vol. 41, no. 1-2, pp. 65-80, 2020.

[2] R. Davalos and B. Rubinsky, "Electrical impedance tomography of cell viability in tissue with application to cryosurgery," *J. Biomech. Eng.*, vol. 126, no. 2, pp. 305-309, 2004.

[3] D.S. Holder, "Electrical impedance tomography (EIT) of brain function," *Brain topography*, vol. 5. No. 2, pp. 87-93, 1992.

[4] M.H. Choi, T.J. Kao, D. Isaacson, G.J. Saulnier and J.C. Newell, "A reconstruction algorithm for breast cancer imaging with electrical impedance tomography in mammography geometry," *IEEE transactions on biomedical engineering*, vol. 54, no. 4, pp. 700-710, 2007.

[5] U.G. Kyle, I. Bosaeus, A.D. De Lorenzo, P. Deurenberg, M. Elia, J.M. Gómez, B.L. Heitmann, L. Kent-Smith, J.C. Melchior, M. Pirlich and H. Scharfetter, "Bioelectrical impedance analysis—part I: review of principles and methods," *Clinical nutrition*, vol. 23, no. 5, pp. 1226-1243, 2004.

[6] D.A. Dean, T. Ramanathan, D. Machado and R. Sundararajan, "Electrical impedance spectroscopy study of biological tissues," *Journal of electrostatics*, vol. 66, no. 3-4, pp. 165-177, 2008.

[7] J. Tang, W. Yin and M. Lu, "Bio-impedance spectroscopy for frozen-thaw of bio-samples: Non-contact inductive measurement and finite element (FE) based cell modelling". *Journal of Food Engineering*, vol. 272, pp.109784, 2020.

[8] C. Tan, S. Liu, J. Jia and F. Dong, "A wideband electrical impedance tomography system based on sensitive bioimpedance spectrum bandwidth," *IEEE Transactions on Instrumentation and Measurement*, vol. 69, no. 1, pp. 144-154, 2019.

[9] M.D. O'Toole, L.A. Marsh, J.L. Davidson, Y.M. Tan, D.W. Armitage and A.J. Peyton, "Non-contact multi-frequency magnetic induction spectroscopy system for industrial-scale bio-impedance measurement," *Measurement Science and Technology*, vol. 26, no. 3, pp.035102, 2015.

[10] A.J. Surowiec, S.S. Stuchly, J.R. Barr, and A.A.S.A. Swarup, "Dielectric properties of breast carcinoma and the surrounding tissues," *IEEE Transactions on Biomedical Engineering*, vol. 35, no. 4, pp. 257-263, 1988.

[11] H. Fricke and S. Morse, "The electric capacity of tumors of the breast," *The Journal of Cancer Research*, vol. 10, no. 3, pp. 340-376, 1926.

[12] J. Jossinet and M. Schmitt, "A review of parameters for the bioelectrical characterization of breast tissue," *Annals of the New York academy of sciences*, vol. 873, no. 1, pp. 30-41, 1999.

[13] T.E. Kerner, K.D. Paulsen, A. Hartov, S.K. Soho and S.P. Poplack, "Electrical impedance spectroscopy of the breast: clinical imaging results in 26 subjects," *IEEE transactions on medical imaging*, vol. 21, no. 6, pp. 638-645, 2002.

[14] J. Gao, S. Yue, J. Chen and H. Wang, "Classification of normal and cancerous lung tissues by electrical impendence tomography," *Bio-medical materials and engineering*, vol. 24, no. 6, pp.2229-2241, 2014.

[15] B.H. Brown, "Electrical impedance tomography (EIT): a review.," *Journal of medical engineering & technology*, vol. 27, no. 3, pp.97-108, 2003.

[16] B. Wang, Y. Hu, H. Ji, Z. Huang and H. Li, "A Novel Electrical Resistance Tomography System Based on $C^4D$ Technique," *IEEE Transactions on Instrumentation and Measurement*, vol. 62, no. 5, pp.1017-1024, 2013.

[17] Y. D. Jiang and M. Soleimani, "Capacitively coupled resistivity imaging for biomaterial and biomedical applications," *IEEE Access*, vol. 6, pp. 27069-27079, 2018.

[18] Y. D. Jiang and M. Soleimani, "Capacitively coupled electrical impedance tomography for brain imaging," *IEEE transactions on medical imaging*, vol. 38, no. 9, pp. 2104-2113, 2019.

[19] G. Ma and M. Soleimani, "Spectral Capacitively Coupled Electrical Resistivity Tomography for Breast Cancer Detection," *IEEE Access*, vol. 8, pp. 50900-50910, 2020.

[20] G. Ma and M. Soleimani, "A New Label-Free and Contactless Bio-Tomographic Imaging with Miniaturized Capacitively-Coupled Spectroscopy Measurements," *Sensors*, vol. 20, no. 11, pp.3327, 2020.

[21] M. Zhang and M. Soleimani, "Simultaneous reconstruction of permittivity and conductivity using multi-frequency admittance measurement in electrical capacitance tomography," *Measurement Science and Technology*, vol. 27, no. 2, pp. 025405, 2016.

[22] Y. Jiang and M. Soleimani, "Capacitively Coupled Phase-based Dielectric Spectroscopy Tomography," *Scientific Reports*, vol. 8, no. 1, pp.1-10, 2018.

[23] Z. Schofield, G.N. Meloni, P. Tran, C. Zerfass, G. Sena, Y. Hayashi, M. Grant, S.A. Contera, S.D. Minteer, M. Kim and A. Prindle, "Bioelectrical understanding and engineering of cell biology.," *Journal of the Royal Society Interface*, vol. 17, no. 166, pp. 20200013, 2020.

[24] C. Gabriel, S. Gabriel and Y.E. Corthout, "The dielectric properties of biological tissues: I. Literature survey," *Physics in medicine & biology*, vol. 41, no. 11, pp. 2231, 1996.

[25] S. Gabriel, R.W. Lau and C. Gabriel, "The dielectric properties of biological tissues: II. Measurements in the frequency range 10 Hz to 20 GHz," *Physics in medicine & biology*, vol. 41, no. 11, pp. 2251, 1996.

[26] H.P. Schwan, "November. Electrical properties of tissues and cell suspensions: mechanisms and models," In *Proceedings of 16th Annual International Conference of the IEEE Engineering in Medicine and Biology Society* (Vol. 1, pp. A70-A71). IEEE, 1994.

[27] K.S. Cole and R.H. Cole, "Dispersion and absorption in dielectrics I. Alternating current characteristics," *The Journal of chemical physics*, vol. 9, no. 4, pp. 341-351, 1941.

[28] H. Fricke, "A mathematical treatment of the electric conductivity and capacity of disperse systems I. The electric conductivity of a suspension of homogeneous spheroids," *Physical Review*, vol. 24, no. 5, pp. 575, 1924.

[29] J.L. Damez, S. Clerjon, S. Abouelkaram, and J. Lepetit, "Dielectric behavior of beef meat in the 1–1500 kHz range: Simulation with the Fricke/Cole–Cole model," *Meat Science*, vol. 77, no. 4, pp. 512-519, 2007.

[30] J.K. Seo, T.K. Bera, H. Kwon and R. Sadleir, "Effective admittivity of biological tissues as a coefficient of elliptic PDE," *Computational and mathematical methods in medicine*, 2013.

[31] Y. Yang, W. Ni, Q. Sun, H. Wen and Z. Teng, "Improved Cole parameter extraction based on the least absolute deviation method," *Physiological measurement*, vol. 34, no.10, pp.1239, 2013.

[32] B.J. Nordbotten, C. Tronstad, Ø.G. Martinsen, and S. Grimnes, "Evaluation of algorithms for calculating bioimpedance phase angle values from measured whole-body impedance modulus," *Physiological measurement*, vol. 32, no.7, pp. 755, 2011.

[33] C. Gunes, Q.M. Marashdeh and F.L. Teixeira, "A comparison between electrical capacitance tomography and displacement-current phase tomography," *IEEE Sensors Journal*, vol. 17, no. 24, pp. 8037-8046, 2017.

[34] J. Xiang, Y. Dong, and Y. Yang, "Multi-Frequency Electromagnetic Tomography for Acute Stroke Detection Using Frequency-Constrained Sparse Bayesian Learning," *IEEE Transactions on Medical Imaging*, vol. 39, no. 12, pp. 4102-4112, 2020.

[35] B. Chen, J.F. Abascal and M. Soleimani, "Electrical resistance tomography for visualization of moving objects using a spatiotemporal total variation regularization algorithm," *Sensors*, vol. 18, no. 6, pp. 1704, 2018.

[36] F. Li, J.F. Abascal, M. Desco and M. Soleimani, "Total variation regularization with split Bregman-based method in magnetic induction tomography using experimental data," *IEEE Sensors Journal*, vol. 17, no. 4, pp. 976-985, 2016.

[37] L. Yang, W. Liu, R. Chen, G. Zhang, W. Li, F. Fu and X. Dong, "In Vivo Bioimpedance spectroscopy characterization of healthy, hemorrhagic and ischemic rabbit brain within 10 Hz–1 MHz," *Sensors*, vol. 17, no. 4, pp.791, 2017.

**GEGE MA** received the B.Eng. degrees in electrical power engineering from the University of Bath, Bath, U.K., and from North China Electrical Power University, Baoding, China, in 2017. She is currently pursuing the Ph.D. degree in electromagnetic tomography for medical imaging. She works as PhD student in Engineering Tomography Lab (ETL) at the University of Bath, Bath, U.K.



**MANUCHEHR SOLEIMANI** received the B.Sc. degree in electrical engineering and the M.Sc. degree in biomedical engineering, and the Ph.D. degree in inverse problems and electromagnetic tomography from The University of Manchester, Manchester, U.K., in 2005. From 2005 to 2007, he was a Research Associate with the School of Materials, The University of Manchester. In 2007, he joined the Department of Electronic and Electrical Engineering, University of Bath, Bath, U.K., where he was a Research Associate and became a Lecturer, in 2008, a Senior Lecturer, in 2013, a Reader, in 2015, and a Full Professor, in 2016. In 2011, he founded the Engineering Tomography Laboratory (ETL), University of Bath, working on various areas of tomographic imaging, in particular multimodality tomographic imaging. He has authored or co-authored well over 300 publications in the field.